Significant oxygen underestimation when quantifying Barium doped SrTiO (Ba:STO) layers by atom probe tomography

Richard J. H. Morris[1], Jhao-Rong Lin[1,2], Jeroen E. Scheerder[1], Mihaela I. Popovici[1], Johan Meersschaut[1], Ludovic Goux[1], Gouri Sankar Kar[1], Paul van der Heide[1] and Claudia Fleischmann[1,2.]

Corresponding Author: richard.morris@imec.be

[1.] imec, Kapeldreef 75, 3001, Leuven, Belgium.

[2.] KU Leuven, Department of Physics and Astronomy, Quantum Solid-State Physics, B-3001 Leuven Belgium.

Abstract

In this paper the capability for quantifying the composition of Ba doped SrTiO (Ba:STO) layers from an atom probe measurement were explored. Rutherford backscattering spectrometry and time-of-flight/energy elastic recoil detection were used to benchmark the composition where the amount of titanium was intentionally varied between samples. The atom probe results showed a significant divergence from the benchmarked composition. The cause was shown to be a significant oxygen underestimation ($\gtrsim$14 at.%). The ratio between oxygen and titanium for the samples varied between 2.6 and 12.7, while those measured by APT were lower and covered a narrower range between 1.4 and 1.7. This difference was found to be associated with the oxygen and titanium predominantly field-evaporating together as a molecular ion. The evaporation fields and bonding chemistries determined showed inconsistences for explaining the oxygen underestimation and ion species measured. The measured ions charge state was in excellent agreement with that predicted by the Kingham post-ionization theory. Only by considering the measured ion species; their evaporation fields; the co-ordination chemistry; the analysis

conditions; and some recently reported density functional theory modelling for oxide field emission, were we able to postulate a field emission and oxygen neutral desorption process which may explain our results.

Introduction

In modern semiconductor devices, there are an increasing number of different oxides which now play a role. These not only include the traditional insulating gate oxides, e.g., SiO_2 through to HfO_2 (Hall et al., 2007; Sharma et al., 2022), but also the more complex transition-metal oxide perovskites like $SrTiO_3$ and $BiFeO_3$ (Ji et al., 2019), being investigated for future memory and quantum computing applications (Pai et al., 2013). Parameters such as the layer thickness, the composition, and the spatial homogeneity i.e., how the different elements are distributed within the layer, can all significantly influence the performance of the final device. Producing these oxide layers requires growth techniques such as atomic layer deposition (ALD) (Popovici et al., 2010) although achieving the optimum structure is challenging. In addition to the growth, accurate characterization for improved learning is also required. This enables the layer properties to be refined and optimized with respect to the device performance. Given the nanometre scale of the oxide layer thicknesses now being sought, the multifarious layer chemistries being explored, and the transition away from 2D i.e., planar technology, to 3D devices, there are few techniques which can offer the combined spatial resolution and mass analysis capabilities needed. An emerging technique that has the potential to meet these challenges is atom probe tomography (APT) (Larson et al., 2016; Gault et al., 2021).

APT enables 3D elemental mapping of a material at sub-nm resolution (Gault et al., 2021). This is achieved by preparing the sample into an ~100 nm diameter needle shaped tip while retaining the region of interest (ROI) close to the apex. The needle shaped tip is then field

evaporated using either a high voltage pulse to vary the electric field at the apex, or ultrafast laser pulses superimposed on a DC voltage which changes the apex temperature. The field emitted ions are then collected on a 2D detector. The ion time of flight i.e., the time the ion takes to go from the tip apex to the 2D detector, enables their mass-to-charge ratio to be determined. The ion arrival sequence is used to determine their depth information. The measured ions are then reconstructed to provide 3D compositional information about the sample (Gault et al., 2021). With the advent of laser assisted APT, the range of materials suitable for APT analysis has evolved from just metals to include semiconductors and insulators. APT offers the potential for accurate compositional accuracy provided that all the constituent atoms making up the sample field evaporate and are detected with the same probability. However, for oxides a commonly reported issue has been the underestimation of the measured oxygen compared to that expected (Marquis et al., 2010; Devaraj et al., 2013; Bachhav et al., 2013; Kinno et al., 2014; Mancini et al., 2014; Devaraj et al., 2015). The objective of this study was to establish if the correct layer composition of barium doped strontium titanate (Ba:STO), a critical parameter for understanding and optimizing its applicability as a device material, was achievable from an APT measurement. However, as the concentration of the titanium was varied significantly for certain samples, the perfect perovskite structure i.e., an ABO_3 type structure, will not always be retained. In this case, other perovskite type structures may form e.g., the Ruddlesden-Popper (RP) phase [Ruddlesden & Popper, 1957; Ruddlesden & Popper, 1958]. The RP phase consists of a two-dimensional perovskite-like layer interleaved with the excess cations i.e., Sr or Ba in our case. Given the likelihood some of our samples will not form the perfect perovskite structure, we refer to our samples as Ba:STO to avoid confusion.

Rutherford backscattering spectrometry (RBS) and time-of-flight/energy elastic recoil detection (ERD) were employed to establish and benchmark the layer composition. A good

agreement between the Ba:Sr:Ti site fraction measured by APT and RBS was found. However, from the APT O:Sr ratio compared with that measured by ERD, the APT analysis was found to be significantly underestimating the amount of oxygen by ~25 at.%. This ultimately resulted in a large compositional bias.

To elucidate on the cause of the oxygen underestimation, we have investigated the measured ion species and ion fraction, the evaporation field values of each ion, and the energy required to remove each ion i.e., the cohesive energy of each ion type. Our findings show that the species evaporation field and cohesive energies were not able to explain the oxygen underestimation or why certain species of ions e.g., TiO molecules, were being preferentially field evaporated. The charge state of the ions was also investigated and found to be in excellent agreement with the Kingham post-ionization theory. Based on our analysis and considering some recently predicted field emission behaviour for MgO or ZnO using DFT modelling (Karahka & Kreuzer, 2013; Karahka & Kreuzer, 2015), we propose a possible field emission process that explains the experimentally observed preferential emission of certain ions as well as the prominent molecular ion formation and the neutral oxygen desorption.

Materials and Methods

For this study, four Ba:STO samples with two different types of layer stack were produced and analysed using APT (Figure 1a). Sample 1 had the Ba:STO layer deposited directly onto a Si substrate while Samples 2, 3 and 4 had an intermediary TiN layer in-between the Si substrate and Ba:STO layer. The Ba:STO was deposited at 250^{o}C by ALD on 300 mm Si wafers using a $Ba(^{t}Bu_3Cp)_2$ $Sr(^{t}Bu_3Cp)_2$ - $Ti(OCH_3)_4$ - H_2O reaction system. As the titanium composition was the parameter of interest, this was varied by changing the saturation condition for the Ti-O sub-cycle during the ALD deposition process. For the layers deposited on 10 nm TiN, a 700^{o}C spike anneal

in a N_2 atmosphere was used to crystallize the films. The layer stacks of Samples 2, 3 and 4 were relevant for memory applications. Sample 1, on the other hand, was intended to have the same Ba:STO layer composition as Sample 2 but allowed the combination of RBS and ERD analysis to be made more precisely. The reason for this was because the Ti from the TiN and Ba:STO layers could not be isolated by RBS for Samples 2, 3 and 4. For Samples 3 and 4, the titanium levels were intentionally varied. Finally, a TiO_2 single crystal was also analysed with APT to aid in understanding the field evaporation of the Ti and O. As the Ba:STO layers were superficial, a Ni capping layer was evaporated onto the samples to protect them during APT tip preparation. All the APT tips used in this study were made using the conventional focused ion beam (FIB) lift-out approach (Miller et al., 2007) with a FEI Helios 450 FIB/SEM. The final tip diameter was in the range of 50 - 100 nm, and a 2 kV (10 pA) Ga beam clean prior to loading the samples into the APT instrument was adopted.

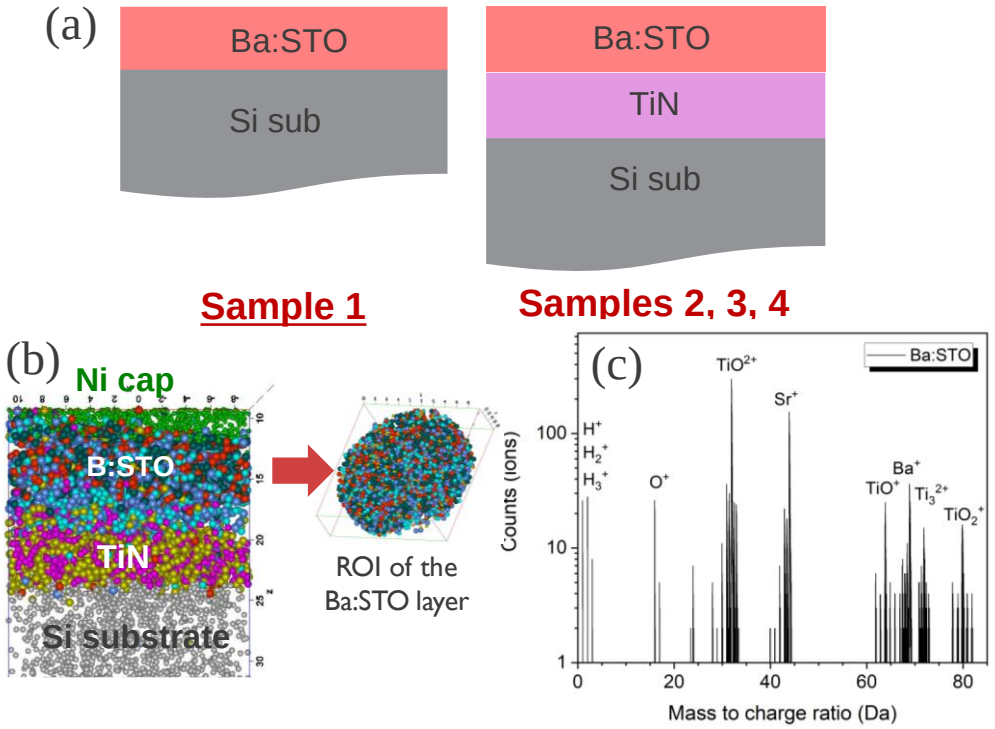

Figure 1. (a) Schematic depiction of the two types of Ba:STO layer samples used in this study, (b) a ROI taken from the APT analysis of Sample 2 showing the different layers and a further ROI just incorporating the Ba:STO layer, and (c) the mass spectrum from just the Ba:STO layer ROI.

The atom probe analysis was performed using either a CAMECA LEAP 5000 XR or LaWaTaP in UV laser mode (λ = 355 nm LEAP and λ = 343 nm LaWaTaP). The laser energy/power (LE/LP) used varied between samples and is therefore reported alongside the *apparent* concentration determined. The base temperature used was 50 K for the LEAP and 80 K for the LaWaTaP analyses. A laser pulse frequency of 125 kHz and 100 kHz were used for the LEAP and LaWaTaP respectively. The *apparent* concentration for all the samples was determined using the CAMECA IVAS 3.8 (LEAP) or TaP3D (LaWaTaP) software and by ranging all the

peaks in the mass spectrum. A significant challenge for the APT analysis of the Ba:STO samples at these laser wavelengths i.e., λ = 343 - 355 nm, was the yield. An estimate for the number of analyses where the data acquisition was not prematurely interrupted by specimen failure was found to be extremely low i.e., in the range of 10 - 20 %.

As already mentioned, a combination of RBS and time-of-flight/energy ERD analysis were used to analyse Sample 1 (Meersschaut & Vandervorst, 2017). For the RBS analysis we used an ion beam of 1.523 MeV He^{+}, a sample tilt of 11° and a scattering angle of 170°, and with the sample rotating along the sample normal to suppress effects from channelling. Thereby, RBS enabled us to accurately determine the relative areal densities of Ba, Sr and Ti. For the time-of-flight/energy ERD analysis a beam of 8 MeV $^{35}Cl^{4+}$ with a sample tilt of 10° and scattering angle 40° was used. The results were verified with time-of-flight/energy ERD measurements using a 10 MeV $^{63}Cu^{5+}$ with a sample tilt of 20° and scattering angle of 40°. The time-of-flight/energy ERD analysis allowed us to accurately determine the relative areal densities of Sr and O for the sample.

Results

Ba:STO APT analysis

A region of interest (ROI) from a voltage reconstructed data set taken from Sample 2 (full device stack measured on the LEAP 5000 XR) is given in Figure 1b. The reconstruction shown was guided by the Ba:STO layer thickness previously determined by transmission electron microscopy to be 7 nm. From the reconstruction the Ni cap, Ba:STO layer, TiN layer, and the underlying Si substrate are observed. In Figure 1b a ROI from just the Ba:STO layer (20 nm diameter and 5 nm in depth) is given, and in Figure 1c we show the corresponding mass spectrum. The mass spectrum given in Figure 1c is highly representative of that found for all the Ba:STO

layer samples. The *apparent* composition as shown in Table I was determined by ranging the mass spectrum peaks and applying peak decomposition, for example, to resolve $^{16}O_2^+$ from $^{48}Ti^{16}O^{++}$. The errors quoted in Table I reflect the 1σ counting statistical uncertainty (Miller & Forbes, 2009). Several mass peaks centred around 72 Da had some ambiguity concerning their identity. Although the peaks had the isotope signature of titanium, they could be attributed to either Ti_3^{++} or $Ti_2O_3^{++}$. The *apparent* layer composition determined and given in Table I assumed that the peaks centred around 72 Da were $Ti_2O_3^{++}$. This assumption was also adopted for all the APT quantification of the Ba:STO samples studied and reported in this paper. To investigate the validity of this choice, two analyses on the data were performed assuming that the peaks were either Ti_3 i.e., favouring more titanium, or Ti_2O_3 molecules i.e., now favouring more oxygen. In fact, the choice of assignment on the *apparent* titanium and oxygen levels was found to be small i.e., of the order of 0.5 at.%. Another ambiguity for the analysis of the m/z spectrum relates to oxygen. The signal in the spectra at a m/z of 16 i.e., 16 Da, may reflect the detection of either O^+ or O_2^{++}. However, as the signal intensity at 16 Da was always very small, the impact of its assignment on the *apparent* oxygen composition determination was minor and of the order of 1 at.%. For the *apparent* concentration values presented in this work, the signal at 16 Da was assumed to originate from O^+.

Table I. *Apparent* composition for Samples 1, 2, 3, 4 and single crystal TiO_2 determined from APT measurements using either the LEAP and LAWATAP.

Sample/instrument/ laser power/energy	Element			
	Ti (at.%)	Ba (at.%)	Sr (at.%)	O (at.%)
Sample 1 (LEAP) LE= 25 pJ	30.5 ± 0.1	4.2 ± 0.1	17.4 ± 0.1	47.9 ± 0.1
Sample 1 (LAWATAP) LP = 15,000 µW	29.9 ± 0.3	4.8 ± 0.1	18.3 ± 0.2	47.0 ± 0.3
Sample 2 (LEAP) LE= 35 pJ	31.5 ± 0.2	4.7 ± 0.1	18.2 ± 0.1	45.6 ± 0.1
Sample 3 (LAWATAP) LP = 15,000 µW	29.2 ± 0.2	12.4 ± 0.1	17.1 ± 0.1	41.3 ± 0.2
Sample 4 (LAWATAP) LP = 15,000 µW	16.1 ± 0.5	36.0 ± 0.6	20.2 ± 0.5	27.7 ± 0.5
TiO_2 (LEAP) LE = 30 pJ	36.18 ± 0.01	-	-	63.82 ± 0.01

The most noticeable and reproducible variant of the APT analysis was the much lower oxygen content which had not been intentionally changed i.e., it was expected to be 60 at.%. As the composition determined by APT is found by ranging the mass spectrum peaks, this could still overlook any elemental bias issues due to measurement/instrument limitations (Mancini et al., 2014; Meisenkothen et al., 2015). Underestimation of oxygen has been reported previously for oxides measured by APT. Examples of this include the work of Kinno *et al.* (Kinno et al., 2014) and Bachhav *et al.* (Bachhav et al., 2013) who found oxygen was underestimated when analyzing SiO_2 and α-Fe_2O_3 respectively. Both groups also used an enhanced ^{18}O oxide approach and came to the same conclusion that the loss was an experimental artifact which could not be explained in terms of an O^+/O_2^{++} peak overlap and misassignment. This is somewhat in agreement with our

results because even by ranging the 16 Da peak as O_2^{++}, a minor (≤1 at.%) change to the apparent composition is found. Devaraj *et al.* (Devaraj et al., 2013) also found an underestimation of oxygen when quantifying MgO and suggested this was caused by the undetectable neutral oxygen emission. The underlying mechanism proposed was the long lifetime of holes that form at the corners of the MgO lattice. This is then believed to lead to oxygen neutrals being formed under UV laser illumination. Mancini *et al.* (Mancini et al., 2014) also reported an underestimation of oxygen for the compositional analysis of MgO and ZnO.

Two types of atom probe instruments (CAMECA LEAP 5000 XR and LaWaTaP) were employed during this study. Establishing if there were any significant instrumental related differences on the *apparent* composition determination was required. Therefore, Sample 1 was measured on both tools for comparison. This was undertaken because significant differences have been previously observed when measuring similar samples on different tool types (Meisenkothen et al., 2015; Martin et al., 2017). From the analysis of Sample 1 measured using both the LEAP and LaWaTaP, the *apparent* Ba:STO layer compositions determined are presented in Table I. We also note that the apex electric field for both analyses were similar (refer to Table III). This was deduced from the $\frac{TiO^{++}}{TiO^{+}+TiO^{++}}$ CSR (the CSR and its relevance will be discussed later in the paper). As the compositions determined were found to be in good agreement, this suggested that a comparison between data collected on either instrument was feasible.

For samples with a well-defined stoichiometry e.g., MgO, ZnO etc., realizing there is an underestimation and for which species is more straightforward. However, as our oxide layer was a thin quaternary phase material, verifying our APT result i.e., whether the low oxygen value was real or a measurement artifact, required confirmation. From an RBS analysis of Sample 1, an accurate ratio between the Ba:Sr:Ti site fractions was obtained (Table II). Time-of-flight/energy

ERD was then used to establish the O:Sr ratio for this sample (Table II). By combining the RBS and time-of-flight/energy ERD elemental fractions the Ba:STO oxide layer was determined to be $Ba_{0.027}Sr_{0.080}Ti_{0.175}O_{0.718}$. The concentration ($C$) of element x (x being either Ba, Sr, Ti or O) is found by using $C_x = \frac{E_x}{E_{Ba}+E_{Sr}+E_{Ti}+E_O}$, where E_{Ba}, E_{Sr} and E_{Ti} are the (RBS) site fractions for the elements Ba, Sr and Ti and $E_o = E_{Sr} \times (O:Sr)_{ERD}$. The amount of oxygen determined i.e., 71.8 ± 2.1 at.%, confirmed that the APT analysis (Table I) had significantly underestimated its presence by ~25 at.%. The RBS and APT analyses (LEAP and LaWaTaP) show a good agreement in terms of the Ba:Sr:Ti site fraction (see Table II). This implies that the Ba, Sr, and Ti are either not being underestimated or, they are all underestimated by a similar amount. However, the O:Sr ratio determined by ERD and APT are very different (Table II). Based on these findings it can therefore be inferred that the significant elemental bias for the analysis using APT of this Ba:STO layer was coming from an oxygen underestimation. A similar behaviour to that found here has been reported for $LiNiMnO_3$ samples (Devaraj et al., 2015). The authors found the measured Li, Mn and Ni concentrations were in good agreement with those expected when they renormalized independently of O.

Table II. Element site fractions for Ba:Sr:Ti determined by APT and RBS; O:Sr ratio found by ERD and APT; Ba:Sr:Ti:O elemental fractions as determined using APT (LEAP and LaWaTaP) and RBS in combination with ERD; the $\frac{Ba+Sr}{Ti}$ fraction.

Sample	Ba:Sr:Ti site fractions			O:Sr ratio	O:Sr ratio	Ba:Sr:Ti:O (at.%)	$\frac{Ba+Sr}{Ti}$
	RBS	LEAP	LAWATAP	ERD	APT (Table I)	ERD corrected	ERD corrected
1		8.0:33.5:58.5		8.98	2.75	2.0:8.4:14.6:75.0	0.71
1			9.1:34.6:56.3	8.98	2.57	2.3:8.4:13.7:75.6	0.78
1	9.5:28.3:62.2			8.98	-	2.7:8.0:17.5:71.8	0.61
2	-	8.7:33.5:57.8	-	4.56	2.50	3.4:13.3:22.9:60.4	0.73
3	-	-	21.1:29.1:49.8	5.47	2.42	8.2:11.2:19.2:61.4	1.01
4	-	-	49.7:28.0:22.3	10.03	1.37	13.1:7.4:5.8:73.7	3.53

As previously mentioned, RBS could not be used for the determination of the Ba:Sr:Ti site fraction for Samples 2, 3 and 4 due to the additional TiN layer. Recalling the good agreement between RBS and APT for these elements in Sample 1 (as shown in Table II), the APT Ba:Sr:Ti site fraction for Samples 2, 3 and 4 were assumed reliable. Time-of-flight/energy ERD was then used to extract an O:Sr ratio (see Table II) for Samples 2, 3 and 4. By combining these APT and Time of flight/ERD ratios, the Ba:STO layer compositions for Samples 2, 3 and 4 were determined and are given in Table II. Although the oxygen content for Samples 2 and 3 were found to be ~60 at.%, while for Sample 4 >60 at.%, it again (refer to Table I) highlights that APT had underestimated the oxygen content. For Samples 2 and 3 this was in the region of ≳14 at.% and for Sample 4 significantly more (of the order of 45 at.%). For completeness we also determined the layer composition for Sample 1 using the APT and Time of flight/ERD elemental fractions. This not only shows excellent agreement between the two APT tools but also with the RBS and ERD composition determination (Table II). The enhanced oxygen observed for Sample 1 and 4 is believed to be linked with the Ba:STO layer growth. This involved a stratum type approach whereby Sr rich TiO and BaO layers were deposited separately and then subsequently annealed at 700^{o} under N_2 to form the Ba:STO layer. It is possible that oxygen containing molecules e.g., OH, CO_2 etc., may have been absorbed, especially if segregation of BaO/SrO occurred (Middleburgh et al., 2013). From the $\frac{Ba+Sr}{Ti}$ fraction (Table II) we also observe an increasing Ba+Sr enrichment compared to Ti as we go from Sample 1 to Sample 4 which was intentional and expected.

TiO_2 APT analysis

In addition to the Ba:STO samples, a single crystal TiO_2 sample was analysed. As this was a bulk sample, a larger amount (~8M) of ions were collected enabling better counting statistics compared to the nanometre Ba:STO layers. From the resulting mass spectrum, an additional set of

peaks centred around 92 Da were now found. These peaks again showed the fingerprint of a titanium presence but could be either Ti_2^{++} or TiO_3^{++}. Assuming these peaks to be TiO_3^{+} i.e., favouring oxygen over titanium, the *apparent* composition was determined to be $Ti_{0.362}O_{0.638}$ (i.e., a O:Ti ratio of 1.76). For this simpler binary sample structure, the APT analysis does show an improved agreement with the expected O:Ti ratio of 2. This also aligns with other binary oxide analyses where a stoichiometry was observed which is in line with the known crystal structure, e.g., TiO_2, HfO_2 (Mutas et al., 2011; Lim et al., 2020). However, although the discrepancy in stoichiometry determined appears to be small, the species underestimated was again oxygen.

Apex field

Previous studies have shown that the sample apex electric field can have a significant influence on the *apparent* composition measured by APT (Mancini et al., 2014; Diercks & Gorman, 2015; Morris et al., 2018; Morris et al., 2019). Thus, to evaluate the comparison between all our samples, some knowledge about the apex electric field was required. Although the apex electric field cannot be measured directly, an indication of the average apex electric field can be inferred through the charge state ratio (CSR) (Kingham, 1982) of an ion species present in the mass spectrum. From our mass spectra both TiO^{+} and TiO^{++} were present. The $\frac{TiO^{++}}{TiO^{+}+TiO^{++}}$ CSR was therefore used to investigate if the apex electric field was comparable between sample analyses. Table III shows the $\frac{TiO^{++}}{TiO^{+}+TiO^{++}}$ CSR values i.e., average apex electric field, found for each sample analysed. For Samples 1-3 and the single crystal TiO_2, the $\frac{TiO^{++}}{TiO^{+}+TiO^{++}}$ CSR was similar. However, for Sample 4 the $\frac{TiO^{++}}{TiO^{+}+TiO^{++}}$ CSR was much lower indicating that any comparisons made with this sample should be treated with caution.

A semi-quantitative estimation of the apex electric field using the post-ionization model of Kingham (Kingham, 1982) was made. Using this post-ionization model to determine the TiO curves, an average apex electric field in the range ~20-22 V/nm was estimated based on the $\frac{TiO^{++}}{TiO^{+}+TiO^{++}}$ CSR for all the samples analysed. Assuming this apex electric field range and determining the Kingham curves for all the other elements/molecules, we find that O, O_2 and TiO_2 should be singly charged while Ba, Sr and Ti doubly charged. These post-ionization predictions are found to be in excellent agreement with our measured data. This therefore appears to indicate that the ions we measure originate in their singly charged form before some undergo post-ionization. From a theoretical study of ZnO field evaporation by Karahka and Kreuzer (Karahka & Kreuzer, 2015), one expects a field dependence for the Zn ion charge state. For an evaporation field of 17 V/nm the authors predicted the emission of Zn^{+} while for 25 V/nm it is Zn^{++}. For the lower field situation where Zn^{+} is predicted to field evaporate, post-ionization was given as the reason for the detection of Zn^{++}. Although our results are in good agreement with the post-ionization theory, we also note that Ba and Sr do have a +II oxidation state within the Ba:STO lattice and so their direct field emission as Ba^{++} or Sr^{++} cannot be ruled out.

Table III. The $\frac{TiO^{++}}{TiO^{+}+TiO^{++}}$ CSR ratio for all the Ba:STO and single crystal TiO_2 samples analysed; the O:Ti ratio taken from the APT analysis (Table I) and ERD corrected data (Table II), and the percentage of ion species contributing to the *apparent* composition determined for each sample.

Sample	$\frac{TiO^{++}}{TiO^{+}+TiO^{++}}$ (%)	O:Ti ratio (Taken from the APT data of Table I)	O:Ti ratio (ERD corrected Table II)	Ion species								
				Ti (%)	TiO_3 (%)	Ti_2O_3 (%)	TiO (%)	TiO_2 (%)	O (%)	O_2 (%)	Ba (%)	Sr (%)
1 (LEAP)	92.1	1.57	5.14	0.4	0.0	5.7	53.7	2.9	2.2	13.5	4.2	17.4
1 (LaWaTaP)	88.4	1.57	5.52	0.3	0.0	4.1	53.9	2.8	1.5	14.3	4.8	18.3
2 (LEAP)	99.0	1.45	2.64	0.3	0.0	6.6	55.6	2.3	0.6	11.7	4.7	18.2
3 (LAWATAP)	82.9	1.41	3.20	0.3	0.0	4.1	53.9	2.8	1.5	14.3	4.8	18.3
4 (LAWATAP)	52.1	1.72	12.71	0.1	0.0	10.7	19.6	7.6	0.1	3.7	37.2	21.0
TiO_2 (LEAP)	88.0	1.76	-	0.7	0.4	2.3	65.0	6.0	1.2	24.4	-	-

Measured ion species

An explanation for the large compositional bias observed was sought through an in-depth investigation of the mass spectra. Additionally, Müller's image hump model (Forbes, 1995) was applied to determine the measured ions (zero barrier) evaporation fields while the ions co-ordination number was employed to extract their individual cohesive energies, both parameters considered to be influential.

Using the ranged mass peaks, the fraction of each ion measured was established and is given in Table III. From Table III we note that the most significant emission for the titanium and oxygen was as a molecular ion e.g., $TiO^{+/++}$, TiO_2^{+}, $Ti_2O_3^{++}$, O_2^{+}. For the strontium and barium, it was as a doubly charged single ion e.g., Sr^{++} and Ba^{++}. From Table III we also see that for Samples 1, 2 and 3 where the apex electric field and titanium levels were comparable, the fraction of each ion type is very similar. For Sample 4 a lower TiO fraction is found. This can be explained based on the lower amount of titanium present and increased barium and strontium levels. This is also supported by considering the APT O:Ti ratio for all four Ba:STO samples which are found to be very similar (Table III). We also note that these O:Ti ratios are not that dissimilar to those found for the single crystal TiO_2 sample i.e., 1.76. This would imply that the titanium and oxygen emission process between these different types of layers i.e., Ba:STO and single crystal TiO_2, is very similar. This includes where we have a significant variation in the titanium composition i.e., by almost a factor 4 as we go from Sample 1 to Sample 4 based on the ERD corrected APT data (Table II).

The detection of molecules containing oxygen when analysing oxides with APT has been reported previously. For example, in Vella *et al.* (Vella et al., 2011) the APT mass spectra presented for both MgO and TiO_2 indicate that the principal mass peaks are MgO_x or TiO_x

molecules. Additionally, in the APT study of ZrO_2 by Dong *et al.* (Dong et al., 2013) the authors claim to readily observe the molecules O_2, ZrO, ZrO_2, and ZrO_2 in their mass spectrum. The mechanism(s) that underpin molecular and to some extent, single ion emission, is still not well understood. To investigate if there was a link between the evaporation field and the single/molecular ions measured, a first order approximation was made by using Müller's image hump model (Forbes., 1995) and Equation 1 for the energy barrier at zero field.

$$Q_0 = E_{coh} + \sum_1^n E_{ion} - n\varphi_e \quad (1)$$

Where E_{coh} is the cohesive energy, n the ionisation state of the ion, $\sum E_{ion}$ the sum of the ionisation energies, and $n\varphi_e$ being n times the work function (φ_e). For this study the energy per bond required to liberate the ion species was adopted for the cohesive energy term. The energy per bond was used because it has previously been reported that the individual atomic bonding arrangement within the structure can be highly influential on the field emission behaviour of oxides (Karahka et al., 2015). For rutile TiO_2, the cohesive energy is given as 19.9 eV/TiO_2 (Hallil et al., 2006) while one unit cell consists of two TiO_2 molecules and 12 Ti-O bonds. The energy per bond is therefore estimated to be 3.32 eV i.e., $\frac{19.9\ eV \times 2}{12\ (bonds)}$. In the case of the Ba:STO it was not possible to find the ionization energies, work function and cohesive energies for different Ba/Sr compositions. Therefore, to obtain an indication of the elemental and molecule ion evaporation field values we have assumed either a $BaTiO_3$ (BTO) or $SrTiO_3$ (STO) layer matrix. For the cubic BTO or STO structures, the respective cohesive energies of 31.57 eV/BTO and 31.70 eV/STO are reported (Uludoĝan et al., 2008). For one unit cell we have either a single BTO or STO molecule consisting of 6 Ti-O bonds and 12 Ba-O or 12 Sr-O bonds respectively. From this we determined the bond energies to be 3.32 eV for the Ti-O (taken from TiO_2) and then either 0.97 eV for Ba-O

or 0.98 eV for Sr-O i.e., $\frac{31.57\ eV-(6\times3.32\ eV)}{12\ (bonds)}=\frac{11.65\ eV}{12\ (bonds)}=0.97\ eV$ per Ba-O bond or $\frac{31.70\ eV-(6\times3.32\ eV)}{12\ (bonds)}=\frac{11.78\ eV}{12\ (bonds)}=0.98\ eV$ per Sr-O bond. For the work function we adopted different values based on a BaO/SrO or TiO_2 terminated surface which are taken from Jacobs (Jacobs et al., 2016). In Figure 2 the measured ion species cohesive energies i.e., energy per bond, the zero-barrier height 1st and 2nd charge state evaporation field values and the 1st and 2nd ionization energies for Ba, Sr, Ti, O, TiO, TiO_2 and O_2 are presented. From the values determined and reported in Tables III and Figure 2, the cohesive energies or the 1st/2nd evaporation field values conflict with the type and fraction of ions measured. For example, although Ba and Sr have the lowest and almost similar evaporation field values, Ti also has a very similar evaporation field but is not among the most abundant ions detected. If anything, it is one of the least abundant. Conversely, the TiO molecule is the most prominent ion detected but its evaporation field value appears to be significantly higher than that of Ba, Sr and Ti. A qualitative agreement does appear to exist for diatomic and elemental oxygen in that they have the highest evaporation field values. This would support the poor field emission resulting in the underestimation of oxygen. However, the findings also suggest that the doubly charged diatomic oxygen i.e., O_2^{++}, should be more favourable compared to singly charged diatomic oxygen i.e., O_2^{+}. This is again not observed i.e., the fraction of O_2^{+} ions far exceed the number of ions measured at 16 Da (Table III).

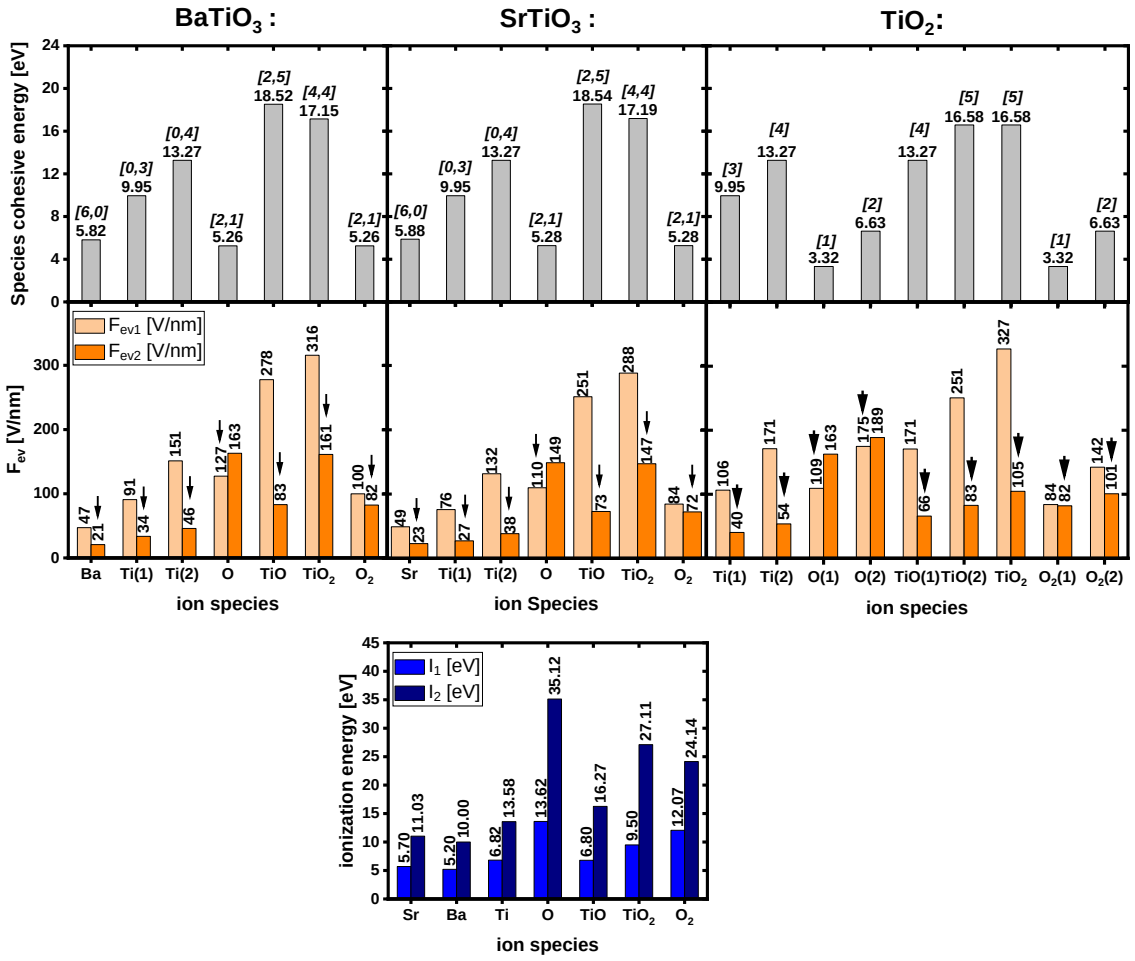

Figure 2. Cohesive energies for the measured ion species determined using the number of bonds (given for BTO and STO in the plots as [Ba/Sr-O,Ti-O] and for TiO_2 [Ti-O]) multiplied by the individual bond energies 0.97 eV (Ba-O), 0.98 eV (Sr-O) and 3.32 eV (Ti-O); the zero-barrier height 1st and 2nd evaporation field (F_{ev}) determined for BTO, STO and TiO_2; The measured ions 1st and 2nd Ionization energies (I_1 & I_2) (Gault et al, 2012) (except I_2 for TiO and TiO_2 which was determined by DFT using the B3LYP/6-311+(d) hybrid density functional/basis set (Gobrecht et al., 2021)). The work functions applied for BTO or STO were 2.78 eV or 3.18 eV for a Ba or Sr rich terminated surface, 5.34 eV (BTO) and 6.33 eV (STO) Ti rich terminated surface while for TiO_2 we used 4.40 eV (Jacobs et al., 2016). The arrows highlight the lowest field of evaporation.

Chemical bonding

Another underlying parameter reported to influence the type of element/molecular ion emission and detection is the chemical bonding (Karahka et al., 2015). Therefore, by considering the number of bonds each element has within the sample structure, the energy required to remove the (molecular) ion species i.e., the cohesive energies, was determined (Figure 2). From these calculations O and O_2 are found to require the least energy although Ba and Sr are similar. Ti was found to need $\gtrsim$ 3 times and TiO and TiO_2 $\gtrsim$ 4 times the energy required to remove O. Based on this, the individual element/molecule cohesive energies do not appear to offer an explanation as to why the most prominent ion measured is TiO.

Density functional theory

More recently, DFT calculations have been adopted to predict the field emission process (Karahka & Kreuzer, 2013; Silaeva et al., 2013; Karahka & Kreuzer, 2015; Gobrecht et al., 2021; Cuduvally et al., 2022). Studies pertinent to this work are those of Karahka (Karahka & Kreuzer, 2013; Karahka & Kreuzer, 2015) who focused on oxide materials. Although Karakha's studies dealt with the simpler MgO and ZnO structures, our more complicated quaternary Ba:STO as well as our single crystal TiO_2 findings do show some similarities. For example, in their model the authors predict the Mg or Zn to field emit first. The sample surface then becomes stretched and buckled which leads to either ZnO or MgO molecules being field emitted. If we were to consider a similar emission behaviour for our samples alongside what we have already determined, then one might expect the Ba and Sr to field emit given their weaker bonds and low evaporation field values. Moreover, the additional weakening impact of polarization should not be overlooked. For a permanent dipole, which exists between Ba-O and Sr-O, and in the presence of a large electric field (tens of volts per nm) like that applied in an APT analysis, ionic polarization would be

expected. A consequence of this polarization effect would include the stretching of the dipole bond (Rosenberg, 1993). As there is typically a correlation between bond length and strength i.e., the larger the bond length the weaker the bond strength, additional bond weakening between the Ba-O or Sr-O atoms through ionic polarization could be expected. This combination of weaker bonds and polarization may also explain why we do not measure any BaO or SrO molecules. Now, following the Ba/Sr field emission, this would give rise to a TiO rich surface. If the upper layer(s) were to then stretch and buckle in a similar way to that predicted by Karakha (Karahka & Kreuzer, 2013; Karahka & Kreuzer, 2015), while the electric field is predicted to penetrate the top layers of an oxide (unlike the case for metals), then any weaker bonds e.g., Ba-O or Sr-O, even if they are sub-surface, could be anticipated to break first. This would result in the field emission of the TiO and TiO_2 molecules from the surface. The emission of the TiO/ TiO_2 molecules would then revert us back to a Ba/Sr rich surface and the process repeats.

Oxygen neutral formation

Returning to the oxygen underestimation and in addition to the field emission of oxygen by TiO/TiO_2 molecules, some oxygen also field evaporates in the form of O_2^+ along with a small amount of O^+. However, even by summing all these our results have shown this does not account for all the oxygen present in the samples. Karakha's (Karahka & Kreuzer, 2015) modelling also predicted that for fields >20 V/nm, molecular oxygen can form on the surface of ZnO. Additionally, for temperatures of >80 K, this molecular oxygen can readily desorb as a neutral. If we consider our analysis conditions alongside these Karakha predictions, a similar reasoning for oxygen neutral desorption can also be made. For instance, the apex electric field based on the $\frac{TiO^{++}}{TiO^{+}+TiO^{++}}$ CSR was estimated to be in the same range as that predicted for molecular oxygen formation on a ZnO surface i.e., ≥20 V/nm. Moreover, the laser energy/power used in this study

can be expected to raise the sample apex temperature above 80 K (Marquis & Gault, 2009; Kumar et al., 2018). For example, the LEAP analysis only requires a modest increase i.e., ≥ 30 K, while for the LaWaTaP measurements, the base temperature was already 80 K before any additional heating from the laser illumination is introduced.

Discussion

From our analysis where we considered some of the key parameters expected to influence the field emission behaviour e.g., the ion cohesive energy, evaporation field values etc., we have shown that these alone cannot describe what we measure from our Ba:STO or single crystal TiO_2 samples. What our studies did show is that the complete field emission of oxygen, in a somewhat similar way to that of nitrogen for many nitrides e.g., GaN, AlN, AlGaN (Mancini et al., 2014; Diercks & Gorman, 2015; Rigutti et al., 2016; Morris et al., 2018; Morris et al., 2019; Morris et al., 2022], remains a significant challenge for APT. Considering the measured ion species determined, we showed that Ti was field evaporated as TiO_x. This resulted in an unexpected correlation between the measured Ti and O concentrations for the Ba:STO layers. Using this correlation, a case for where the significant oxygen underestimation arise from can be made. Firstly, the TiO_x ion emission infers that the oxygen atoms within the sample and bonded to a titanium atom are field emitted and detected. Conversely, the barium and strontium were found to field evaporate as single ions. This implies that the oxygen atoms bonded to the Ba and Sr remain behind. Through this field evaporation process the Ti, Sr and Ba are field emitted and accounted for, which is in good agreement with our findings. However, following the field evaporation of the Sr^{++}/Ba^{++}, it is believed that the oxygen left behind is not accounted for because it (thermally) desorbs as a neutral. This explanation is best observed by considering Sample 4 where we have an

increased Ba/Sr content at the expense of Ti, but also find the largest oxygen underestimation. Figure 3 offers an illustration for the proposed Ba:STO field evaporation process discussed above.

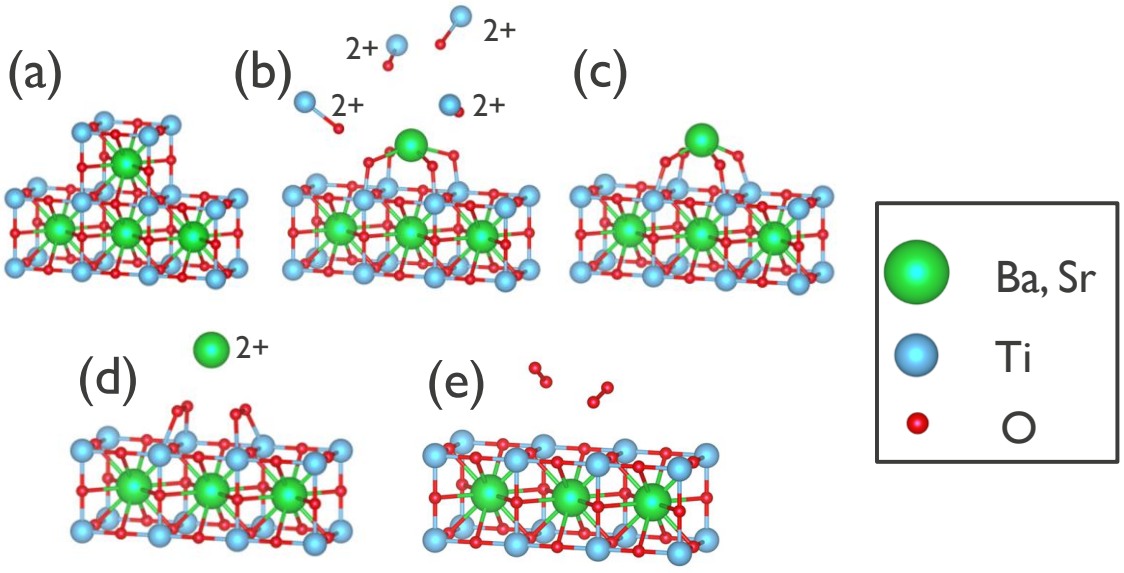

Figure 3. Sketch illustrating the proposed field evaporation behaviour for the Ba:STO layers (a) the sample structure (assuming a perovskite structure); (b) Field evaporation of the TiO^{2+} leaving behind a Ba/Sr rich surface; (c) the Ba/Sr-O bonds become stretched due to ionic polarization caused by the field; (d) Ba^{2+}/Sr^{2+} are field evaporated; (e) The oxygen left behind is then thermally desorbed as neutrals.

If we now consider the single crystal TiO_2 analysis, a much closer agreement to the expected stoichiometry was found i.e., a O:Ti ratio of ~1.76. Again, the correlated Ti and O field evaporation behaviour i.e., in the form of TiO_x, explains the improved agreement with the expected stoichiometry. The O:Ti ratio for the single crystal TiO_2 was found to differ from that expected by ~14%, with the oxygen being the element underestimated. From the APT literature for other binary oxides, one can find similar differences in element ratio reported. Examples include Al_2O_3 where

the O:Al ratio differs by ~15% from that expected (Marquis et al., 2010). For an α-Fe_2O_3 sample Bachhava et al (Bachhav et al., 2013) found their O:Fe ratio was ~10% different to that expected. Kinno et al (Kinno et al., 2014) reported for SiO_2 an O:Si ratio discrepancy in the range of ~8-14% depending on the analysis conditions used. Moreover, what is also evident from these results is that whenever there is a ratio difference reported, oxygen underestimation appears to be the cause. A systematic study to collate the APT element ratio for different benchmarked binary, ternary, quaternary …. etc oxides, along with the analysis conditions, would offer a more robust understanding about which oxides and elements suffer the most zero-barrier evaporation field bias. The preferential underestimation of a species not only affects the composition analysis as we have shown here but, will also have a detrimental impact on the final reconstruction.

Some potential approaches to improve the APT analysis of oxides could include exploring higher apex fields, tip temperature or even the laser wavelength applied. Previous studies have found that higher apex electric field appears to yield a more accurate result (Agrawal et al., 2011; Morris et al., 2018, Morris et al., 2019; Cuduvally et al., 2020; Morris et al., 2022), although increasing the apex electric field too far can also lead to detrimental effects e.g., sample (micro) fracture, (Prosa et al., 2019). Another parameter to consider is the tip temperature. As the field evaporation for laser assisted APT is a thermally driven process (Tsong., 1984; Cerezo et al., 2006), especially when using laser wavelengths in the range λ = 343 - 355 nm (Chiaramonti et al., 2020), determining an athermal approach might offer a solution. Some promising results using extreme ultraviolet (λ = 29.6 nm) laser radiation have recently been reported for the APT analysis of SiO_2 (Chiaramonti et al., 2020). The authors showed that the measured stoichiometry did not significantly deviate from that expected and found it to be invariant of the base temperatures (25 - 150 K) applied. It was proposed that the field evaporation at this wavelength invokes

additional athermal ionization and desorption pathways which do not exist when using current APT laser wavelengths for analysing semiconductors and insulators. As our Ba:STO layers were extremely thin, investigating different analysis conditions was not feasible. However, exploring the impact of different analysis conditions, as discussed above e.g., the apex electric field, laser wavelength, laser pulse frequency etc. would be a logical next step although suitable i.e., thicker Ba:STO layers, are required.

Combining experimental findings with theoretical modelling to better understand the field evaporation process should also not be understated. Our initial attempt to explain our data by using and exploring the simple image hump model proved insufficient. However, from some DFT reported in the literature (Silaeva et al., 2013; Karahka & Kreuzer, 2013; Karahka & Kreuzer, 2015) about the kinetics of field evaporation, albeit for different types of oxide, we were able to postulate on the field evaporation process and oxygen loss observed for our samples. This indicates that DFT offers a very promising route for predicting field evaporation behaviour. However, DFT is not straightforward to implement. For example, executing DFT analysis on sufficiently large atomic arrays that are representative and informative, not just about the initial field evaporation of the surface but also as it proceeds with depth, is extremely time consuming and computer intensive. Moreover, a suitable minimal wave function basis needs to be established. This typically involves studying the effects of a large electric field on the structure using different functionals to determine parameters such as bond lengths, ionisation, and dissociation energies, which are then compared to experimental values reported in the literature.

Conclusions

In this paper we showed a significant compositional bias when analysing Ba:STO layers using APT. The reason was determined to be a ≳14 at.% oxygen underestimation. While the O:Ti

ratio for our samples was intentionally varied by a factor of ~4, the *apparent* O:Ti ratios measured by APT were all similar, as most of the Ti predominantly field-evaporated with O in the form of a TiO_x molecular ion. A simple consideration of the elemental and molecular evaporation field values and/or cohesive energies were not able to explain the type of ions measured, being mostly TiO molecules, nor to explain the oxygen underestimation. However, the charge state of all the ions measured agreed with the Kingham post-ionization theory. By combining our findings with some DFT field emission behaviour of oxides reported in the literature, we were able to propose a plausible explanation for our measured data.

Acknowledgments

The authors acknowledge the financial support by FWO Hercules through project ZW13_09. RM would like to thank David Gobrecht for calculating the 2nd adiabatic ionization energies of TiO/TiO_2.

References

Agrawal, R., Bernal, R.A., Isheim, D &, Espinosa, H.D. (2011). Characterizing Atomic Composition and Dopant Distribution in Wide Band Gap Semiconductor Nanowires Using Laser-Assisted Atom Probe Tomography, J. Phys. Chem. C 115 17688-17694.

Bachhava, M., Danoix, F., Hannoyer, B., Bassat, J.M. & R. Danoix, R. (2013). Investigation of O-18 enriched hematite (α-Fe_2O_3) by laser assisted atom probe tomography, Int. J. Mass Spectrom. **335** 57-60.

Cerezo, A, Smith, G.D.W., & Clifton P.H. (2006). Measurement of temperature rises in the femtosecond laser pulsed three-dimensional atom probe. Appl Phys Lett 88, 154103.

Chiaramonti, A.N., Miaja-Avila, L., Caplins, B.W., Blanchard, P.T., Diercks, D.R., Gorman, B.P., & Sanford, N.A. (2020). Field Ion Emission in an Atom Probe Microscope Triggered by Femtosecond-Pulsed Coherent Extreme Ultraviolet Light, Microsc. Microanal. **26** 258-266.

Cuduvally, R., Morris, R.J.H., Ferrari, P., Bogdanowicz, J., Fleischmann, C., Melkonyan, D. & Vandervorst, W. (2020). Potential sources of compositional inaccuracy in the atom probe tomography of $In_xGa_{1-x}As$, Ultramicroscopy **210** 112918.

Cuduvally, R., Morris, R.J.H., Oosterbos, G., Ferrari, P., Fleischmann, C., Forbes, R.G. & Vandervorst, W. (2022). Post-field ionization of Si clusters in atom probe tomography: A joint theoretical and experimental study. J. App. Phys. **132** 074901.

Devaraj, A., Colby, R., Hess, W.P., Perea, D.E. & Thevuthasan, S. (2013). Role of Photoexcitation and Field Ionization in the Measurement of Accurate Oxide Stoichiometry by Laser-Assisted Atom Probe Tomography. J. Phys. Chem. Lett. **4** 993-998.

Devaraj, A., Gu, M., Colby, Yan, P., Wang, C.M., Zheng, J.M., Xiao, J., Genc, A., Zhang, J.G., Belharouak, I., Wang, D., Amine, K, & Thevuthasan, S. (2015). Visualizing nanoscale 3D compositional fluctuation of lithium in advanced lithium-ion battery cathodes. Nat Commun **6** 8014.

Diercks, D.R. & Gorman, B.P. (2015). Nanoscale measurement of laser-induced temperature rise and field evaporation effects in CdTe and GaN. J. Phys. Chem. C **119** 20623-20631.

Dong, Y., Motta, A.T. & Marquis, E.A. (2013). Atom probe tomography study of alloying element distributions in Zr alloys and their oxides, J. Nucl. Mater. **442** 270–281.

Gault, B., Chiaramonti, A., Cojocaru-Mirédin, O., Stender, P., Dubosq, R., Freysoldt, C., Makineni, S.K., Li, T., Moody, M.P. & Cairney, J.M. (2021). Atom Probe Tomography, Nat Rev Methods Primers 1-51.

Gault, B., Moody, M.P., Cairney, J.M. & Ringer, S.P. (2012). in Atom Probe Microscopy, Eds Hull, R., Jagadish, C., Osgood, R.M., Parisi, Jr.J & Wang, Z.M. Springer series in materials science, New York, NY: Springer New York, 2012.

Gobrecht, D., Sindel, J.P., Lecoq-Molinos, H. & Decin, L. (2021). The Ionization Energies of Dust-Forming Metal Oxide Clusters. Universe **7** 1-11.

Hall, S., Buiu, O., Mitrovic, I.Z., Yi Lu, Yi. & Davey, W.M. (2007). Review and perspective of high-*k* dielectrics on silicon, J. Telecommun. Inf. Technol. **2** 33-43.

Hallil, A., Tétot, R., Berthier, F., Braems, I. & Crueze, J. (2006). Use of variable-charge interatomic potential for atomistic simulations of bulk oxygen vacancies, and surfaces of rutile TiO_2, Phys. Rev. B **73** 165406.

Jacobs, R., Booske, J. & Morgan, D. (2016). Understanding and Controlling the Work Function of Perovskite Oxides Using Density Functional Theory, Adv. Funct. Mater. **26** 5471-5482.

Ji, D., Cai1, S., Paudel, T.R., Sun, H., Zhang, C., Han, L., Wei1, Y., Zang, Y., Gu1, M., Zhang, Y., Gao, W., Huyan, H., Guo1, W., Wu1, D., Gu1, Z., Tsymbal, E.Y., Wang, P., Nie, Y. & Pan, X. (2019). Freestanding crystalline oxide perovskites down to the monolayer limit, Nature 570 87-100.

Karahka, M & Kreuzer, H.J. (2013). Field evaporation of oxides: A theoretical study, Ultramicroscopy **132** 54-59.

Karahka, M & Kreuzer, H.J. (2015). Field evaporation of insulators and semiconductors: Theoretical insights for ZnO, Ultramicroscopy **159** 156-161.

Karahka, M., Xia, Y. & Kreuzer, H.J. (2015). The mystery of missing species in atom probe tomography of composite materials, Appl. Phys. Lett. **107** 062105.

Kingham, D.R. (1982). The post- ionization of field evaporated ions: a theoretical explanation of multiple charge states. Surf. Sci. **116** 273–301.

Kinno, T., Tomita, M., Ohkubo, T., Takeno, S. & Hono, K. (2014). Laser-assisted atom probe tomography of 18O-enriched oxide thin film for quantitative analysis of oxygen. Appl. Surf. Sci. **290** 194-198.

Kumar, A., Bogdanowicz, J., Demeulemeester, J., Bran, D., Melkonyan, D., Fleischmann, C. & Vandervorst, W. (2018). Measurement of the apex temperature of a nanoscale semiconducting field emitter illuminated by a femtosecond laser pulse, Journal of Applied Physics **124** 245105.

Larson, D.J., Prosa, T.J., Perea, D.E., Inoue, K. & Mangelinck, D. (2016). Atom probe tomography of nanoscale electronic materials, MRS Bulletin. **41** 30-34.

Lim, J., Kim, Se-Ho., Armengol, R.A., Kasian, O., Choi, Pyuck-Pa., Stephenson, L.T., Gault, B. & Scheu, C. (2020). Atomic-Scale Mapping of Impurities in Partially Reduced Hollow TiO2 Nanowires, Angew. Chem. Int. Ed. **59** 5651 –5655.

Mancini, L., Amirifar, N., Shinde, D., Blum, I., Gilbert, M., Vella, A., Vurpillot, F., Lefebvre, W., Lardé, R., Talbot, E., Pareige, P., Portier, X., Ziani, A., Davesnne, C., Durand, C., Eymery, J., Butté, R., Carlin, J-F., Grandjean, N. & Rigutti, L. (2014). Composition of wide bandgap semiconductor materials and nanostructures measured by atomprobe tomography and its dependence on the surface electric field, J. Phys. Chem. C. **118** 24136-2416.

Marquis, E.A. & Gault, B. (2009). Determination of the tip temperature in laser assisted atom-probe tomography using charge state distributions, J. Appl. Phys. **104** 084914.

Marquis, E.A., Yhaya, N.A., Larson, D.J., Miller, M.K., & Todd, R.I. (2010). Probing the improbable: imaging C atoms in alumina, Materials Today. 13 34-36.

Martin, T., London, A.J., Jenkins, B., Hopkin, S.E., Douglas, J.O., Styman, P.D., Bagot, P.A.J. & Moody, M.P. (2017). Comparing the Consistency of Atom Probe Tomography Measurements of Small-Scale Segregation and Clustering Between the LEAP 3000 and LEAP 5000 Instruments. Microsc. Microanal. **23** 227-237.

Meersschaut, J & Vandervorst, W. (2017). High-throughput ion beam analysis at imec. Nucl. Instrum. Methods Phys. Res., B. **406**, 25-29.

Meisenkothen, F., Steel, E.B., Prosa, T.J., Henry, K.T. & Kolli, R.P. (2015). Effects of detector dead-time on quantitative analyses involving boron and multi-hit detection events in atom probe tomography. Ultramicroscopy **159** 101-111.

Middleburgh, S.C., Lagerlof, K.P.D. & Grimes, R.W. (2013). Accommodation of Excess Oxygen in Group II Monoxides, J. Am. Ceram. Soc. **96** 308-311.

Miller, M.K. & Forbes, R.G. (2009) Atom Probe Tomography, Mater. Charact. **60** 461-469.

Miller, M.K., Russell, K.F., Thompson, K., Alvis, R & Larson, D.J. (2007). Review of atom probe FIB-based specimen preparation methods, Microsc. Microanal. **13** (6) 428–436.

Morris, R.J.H., Cuduvally, R., Lin, J-R., Zhao, M., Vandervorst, W., Thuvander, M. & Fleischmann, C. (2022). Field dependent study on the impact of co-evaporated multihits and ion pile-up for the apparent stoichiometric quantification of GaN and AlN. Ultramicroscopy **241** 113592.

Morris, R.J.H., Cuduvally, R., Melkonyan, D., Fleischmann, C., Zhao, M., Arnoldi, L., Heide, P. van der & Vandervorst, W. (2018). Toward accurate composition analysis of GaN and AlGaN using atom probe tomography, J. Vac. Sci. Technol. B. **36(3)**, 03F130-1.

Morris, R.J.H., Cuduvally, R., Melkonyan, D., Zhao, M., Heide, P. van der & Vandervorst, W. (2019)., Atom probe of GaN/AlGaN heterostructures: the role of electric field, sample crystallography and laser excitation on quantification, Ultramicroscopy **206** 112813.

Mutas, S., Klein, C. & Gerstl, S.S.A. (2011). Investigation of the analysis parameters and background subtraction for high-k materials with atom probe tomography, Ultramicroscopy **111** 546–551.

Pai, Y-Y,. Tylan-Tyler, A., Irvin, P & Levy, J. (2018). Physics of $SrTiO_3$-based heterostructures and nanostructures: a review, Rep. Prog. Phys. **81** 036503-036556.

Popovici, M., Van Elshocht, S., Menou, M., Swerts, J., Pierreux, D., Delabie, A., Brijs, B., Conard, T., Opsomer, K., Maes, J.W., Wouters, D. J & Kittl, J. A. (2010). Atomic Layer Deposition of Strontium Titanate Films Using $Sr(^tBu_3Cp)_2$ and $Ti(OMe)_4$, J. Electrochem. Soc. **157** G1-G6.

Prosa, Ty J., Strennen, S., Olson, D., Lawrence, D. & Larson, D.J. (2019). A Study of Parameters Affecting Atom Probe Tomography Specimen Survivability, Microsc. Microanal. **25** 425–437.

R. G. Forbes, R.G. (1995). Field evaporation theory: a review of basic ideas, Appl. Surf. Sci. **87/88** 1-11.

Rigutti, L., Mancini, L., Hernández-Maldonado, D., Lefebvre, W., Giraud, E., Butté, R., Carlin, J.F., Grandjean, N., Blavette, D. & Vurpillot, F. (2016). Statistical correction of atom probe tomography data of semiconductor alloys combined with optical spectroscopy: The case of Al0.25Ga0.75N. J. Appl. Phys. **119** 105704.

Rosenberg, H.M. (1993). The Solid State 3rd Ed, Oxford University Press.

Ruddlesden, S.N. & Popper, P. (1957). New compounds of the K_2NiF_4 type, Acta Cryst. **10** 538-55.

Ruddlesden, S.N. & Popper, P. (1958). The compound $Sr_3Ti_2O_7$ and its structure, Acta Cryst. **11** 54-55.

Sharma, U., Kumar, G., Mishra, S. & Thomas, R. (2022). Advancement of Gate Oxides from SiO_2 to High-k Dielectrics in Microprocessor and Memory, J. Phys.: Conference Series **2267** 012142.

Silaeva, E.P., Karahka, M. & Kreuzer, H.J. (2013). Atom Probe Tomography and field evaporation of insulators and semiconductors: Theoretical issues, Current Opinion in Solid State and Materials Science **17** 211–216.

Tsong T.T. (1984). Pulsed-laser-stimulated field ion emission from metal and semiconductor surfaces: A time-of-flight study of the formation of atomic, molecular, and cluster ions, Phys Rev B 30, 4946–4961.

Uludoĝan, M., Guarin, D.P., Gomez, Z.E., Cagin, T. & Goddard III, W.A. (2008). DFT Studies on Ferroelectric Ceramics and Their Alloys: $BaTiO_3$, $PbTiO_3$, $SrTiO_3$, $AgNbO_3$, $AgTaO_3$, $Pb_xBa_{1-x}TiO_3$ and $Sr_xBa_{1-x}TiO_3$, III2CMES 24 215-238.

Vella, A., Mazumder, B., Da Costa G. & Deconihout, B. (2011). Field evaporation mechanism of bulk oxides under ultra-fast laser illumination, J. Appl. Phys. **110** 044321-7.